

Flexural performance of curved-pultruded GFRP arch beams subjected to varying boundary conditions

TianQiao Liu^{a,b,*}, Peng Feng^c, Yulei Bai^{a,b}, Shangcong Bai^a, Jia-Qi Yang^d, Fei Zhao^e

^a Department of Civil Engineering, Beijing University of Technology, Beijing, China

^b State Key Laboratory of Bridge Engineering Safety and Resilience, Beijing University of Technology, Beijing, China

^c Department of Civil Engineering, Tsinghua University, Beijing, China

^d School of mechanics and civil engineering, China university of Mining and Technology, Beijing, China

^e School of Civil Engineering and Architecture, Hainan University, Haikou, China

ARTICLE INFO

Keywords:

Curved-Pultruded GFRP Arch Beam
Beam-String Structure
Flexural Performance
Progressive Failure
Web Crippling Behavior

ABSTRACT

The low stiffness of pultruded glass fiber reinforced polymer (pGFRP) flexural members has been one of the main issues limiting their possible applications ever since this type of material was invented. In this regard, curved-pultrusion technique is adopted in this work to produce GFRP arch beams, and a new GFRP beam-string structure is proposed. Specifically, experimental, numerical, and analytical programs were conducted to investigate the flexural performance of curved-pultruded GFRP arch beams subjected to varying boundary conditions. The flexural strength and stiffness were successfully enhanced by up to 27% and 109%, respectively, which was attributed to the arch mechanism enabled by proposed GFRP beam-string structure. In addition, the progressive failure of GFRP material and the imperfect load-transfer between GFRP arch beam and tension string were investigated through finite element modeling. Then, web crippling strength of GFRP arch beams was predicted with modifications to an existing model, and internal forces of beam-string were analyzed. The GFRP beam-string structure proposed in this work effectively sheds light on possible approach to improve the flexural stiffness of pGFRP members, and with successful demonstration of this work, it is rationally believed that possible applications of curved-pultruded GFRP members can be greatly broadened.

1. Introduction

Pultruded glass fiber reinforced polymer (pGFRP) composites have received an increasing number of interests from construction, automotive, and energy industries all over the world in past two decades [1–5]. Favorable features of pGFRPs that really impress the industries include the high strength- and stiffness-to-weight ratios, excellent corrosion resistance, and superior fatigue performance [6–9]. To date, one of the main issues limiting further applications of pGFRPs is the relatively low modulus of elasticity of material, which is often interpreted as the low stiffness when speaking of structural members. The low stiffness is typically manifested in two aspects, stability and deflection [10]. Stability behaviors (i.e., buckling) of pGFRP members have been extensively investigated by many researchers, and the stability limit state can be readily satisfied provided appropriate plate/member slenderness ratios and/or additional restraints [11–17]. On the other hand, deflection limit state is often found to be the dominant factor in practical

design of pGFRP beams, since flexural members may suffer from excessive deflections under service loads [18].

Conventional pultrusion technique only permits straight profiles and enlarging the cross-sectional geometry might render the only approach to improve the flexural stiffness, if excluding the composite action by pGFRPs and other types of materials [19–24]. In this regard, the present authors [25] have proposed to adopt the curved-pultrusion technique to enable a camber in beams (see Fig. 1a), such that the adverse deflections can be mitigated and the clearance under beams can be ensured. Using curved-pultruded GFRP profiles, a pedestrian bridge spanning over 20 m has been designed and constructed in Beijing, China in 2021, as shown in Fig. 1b. The bridge consists of 20 I-beams, each having geometries of 600 × 200 × 20 × 15 mm (depth × width × flange thickness × web thickness). It is noted that the boundary condition of this bridge is close to simply-supported, and thus, the cambered pGFRP beam (referred to as curved-pultruded GFRP arch beam or short as GFRP arch beam in this work) behaves essentially in the same manner with a simply-supported

* Corresponding author at: Department of Civil Engineering, Beijing University of Technology, Beijing, China.

E-mail address: liu_tianqiao@bjut.edu.cn (T. Liu).

<https://doi.org/10.1016/j.engstruct.2024.117962>

Received 7 January 2023; Received in revised form 27 February 2024; Accepted 31 March 2024

Available online 6 April 2024

0141-0296/© 2024 Elsevier Ltd. All rights reserved.

straight beam.

The most attractive feature of curved-pultruded GFRP profiles, from the perspective of authors, may lie in the possible arch mechanism and its excellent structural performance, especially the improved flexural stiffness. To enable the arch mechanism, in this work a pair of steel tension strings are introduced to curved-pultruded GFRP arch beam, thus making it a beam-string structure, as shown in Fig. 2. In available literature, a CFRP beam-string structure has been reported, which demonstrates an excellent structural efficiency in terms of strength-to-weight ratio [26]. With that said, the flexural performance of simply-supported GFRP arch beam (as control specimen) and the GFRP beam-string structures with varying tensions in strings are investigated. First, a series of experimental program is carried out with respect to 1) small-scale coupons for defining the mechanical properties of material and 2) large-scale beams for determining the flexural strength and stiffness of curved-pultruded GFRP arch beams. Second, finite element modeling is conducted to evaluate and validate the flexural behaviors of beams observed in experimental tests. Third, analytical program is conducted to calculate the ultimate strength as well as internal forces of GFRP arch beams. The GFRP beam-string structure proposed in this work successfully demonstrates an effective approach for enhancing the flexural stiffness as well as increasing the possible span length of pultruded GFRP beams/structures.

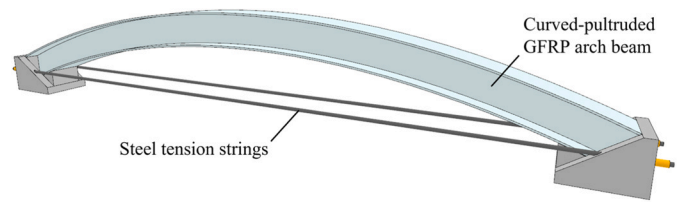
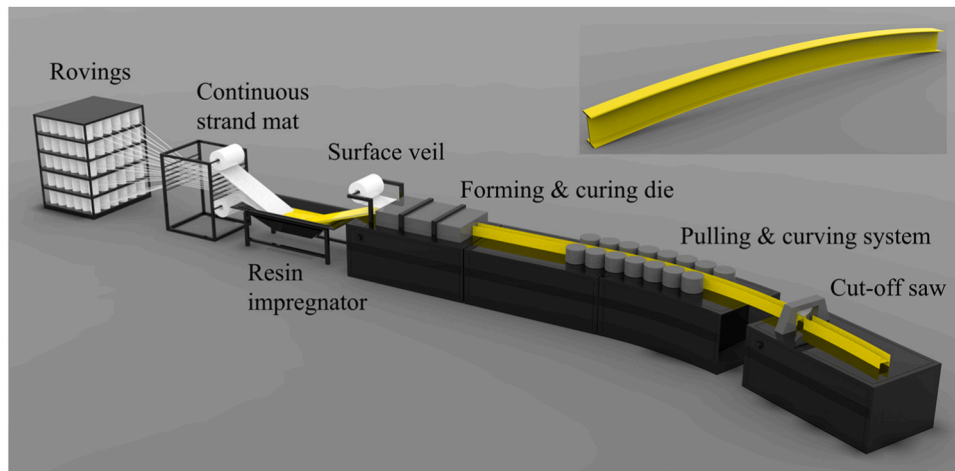


Fig. 2. Proposed GFRP beam-string structure.

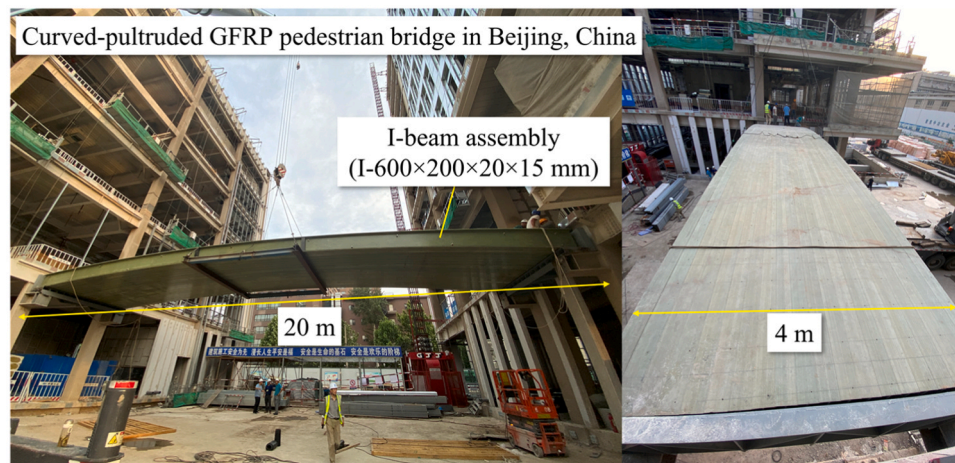
2. Experimental program

2.1. Materials

In this work, the curved-pultruded GFRP arch beams are in form of an I-section with geometries of $100 \times 100 \times 10$ mm (depth \times width \times plate thickness), and they are manufactured by XingTai HongBang Composites Manufacturing Co., LTD., in China. The GFRP materials consist of E-glass fibers and epoxy resin. A series of material characterization tests were conducted to measure the mechanical properties and fiber volume fraction of material. ASTM standard tests as well as the standard coupon geometries were adopted, including D3039 [27] for tensile properties, D6641 [28] for compressive properties, D5379 [29] for in-plane shear properties, D7264 [30] for flexural properties, and D2584 [31] for fiber volume fraction. Those coupons were randomly extracted from top and bottom flanges. Test set-ups and representative



(a) Schematic of curved-pultrusion technique



(b) Curved-pultruded GFRP pedestrian bridge

Fig. 1. Curved-pultrusion technique and its bridge application [25].

failure modes are presented in Fig. A.1. in Appendix A. It is noted that non-standard coupons with geometries of $80 \times 15 \times 10$ mm (length \times width \times thickness) were used for measuring the transverse tensile properties, and these coupons were extracted from web plate.

The experimentally-determined mechanical properties and fiber volume fraction of GFRP materials are summarized in Table 1. All types of properties were successfully obtained with coefficients of variation (COV) less than 0.10, except for in-plane shear modulus and minor Poisson's ratio. With that said, the mechanical properties of top and bottom flanges of curved-pultruded GFRP I-section were about the same, despite of having different curvatures from manufacturing process. In addition, an abnormal data is found for longitudinal tensile strength, which is only 574 MPa, even smaller than longitudinal compressive strength, 647 MPa. This is mainly due to the failure mode observed in 10-mm-thick longitudinal coupons, which is dominated by longitudinal delamination—an interface- and/or matrix-dominated failure mode. According to ASTM D3039, standard coupon thickness is taken equal to as-received thickness of GFRP profiles; however, the thick coupon addressed in this work is observed not to exhibit the fiber-dominated failure mode (i.e., fiber fracture). In this regard, many FRP practitioners often use a milling machine to cut the longitudinal coupon thinner (in thickness direction) or narrower (in width direction) depending on whether the through-thickness architecture is of critical design concern. Although the thinner/narrower coupon can be conveniently tested, the obtained results are susceptible to be at the high-end because of the size effect. In addition, ASTM D638 [32] prescribes to use dog-boned coupons, while it also suggests testing continuous fiber reinforced polymer composites per D3039 (see Note 4 in Section 1.3 of D638). In order to address this issue, standard tests need to be revised in order to accommodate the thick/high-strength materials for heavy-duty purposes emerged in recent years, such as the 20-mm-thick flange plate of bridge I-girder (see Fig. 1b), and the spar cap plates having tensile strength exceeding 1000 MPa. In this work, the longitudinal flexural strength, 808 MPa, is taken as the longitudinal strength of material, and this value is used throughout the following analyses.

2.2. Flexural tests

A total of 12 GFRP arch beams having radius of curvature of 2586 mm were tested under three-point bending test configuration, as shown in Fig. 3. All beams were seated at a pair of customized steel supports. The steel support was designed to accommodate the curvature of beams as well as to allow the anchorage of steel tension strings. Three beams were tested without tension strings; thus, they were simply-supported arch beams and taken as control specimens. The other nine beams were tested with tension strings, making them beam-string structures. Given beam-string structure is a self-balanced structural system, the beam-string specimens were also subjected to simply-

Table 1
Experimentally-determined mechanical properties of GFRP material.

Mechanical properties	Values	COVs
Longitudinal tensile strength F_{Lt} (MPa)	574	0.08
Longitudinal tensile modulus E_{Lt} (MPa)	47208	0.04
Transverse tensile strength F_{Tt} (MPa)	45	0.09
Transverse tensile modulus E_{Tt} (MPa)	14765	0.03
Longitudinal compressive strength F_{Lc} (MPa)	647	0.03
Longitudinal compressive modulus E_{Lc} (MPa)	44770	0.06
Transverse compressive strength F_{Tc} (MPa)	152	0.02
Transverse compressive modulus E_{Tc} (MPa)	13305	0.06
Longitudinal flexural strength F_{Lb} (MPa)	808	0.07
Longitudinal flexural modulus E_{Lb} (MPa)	46763	0.05
In-plane shear strength F_{LT} (MPa)	84	0.09
In-plane shear modulus G_{LT} (MPa)	4573	0.15
Major Poisson's ratio ν_{LT}	0.29	0.03
Minor Poisson's ratio ν_{TL}	0.10	0.15
Fiber volume fraction V_f	0.59	0.01

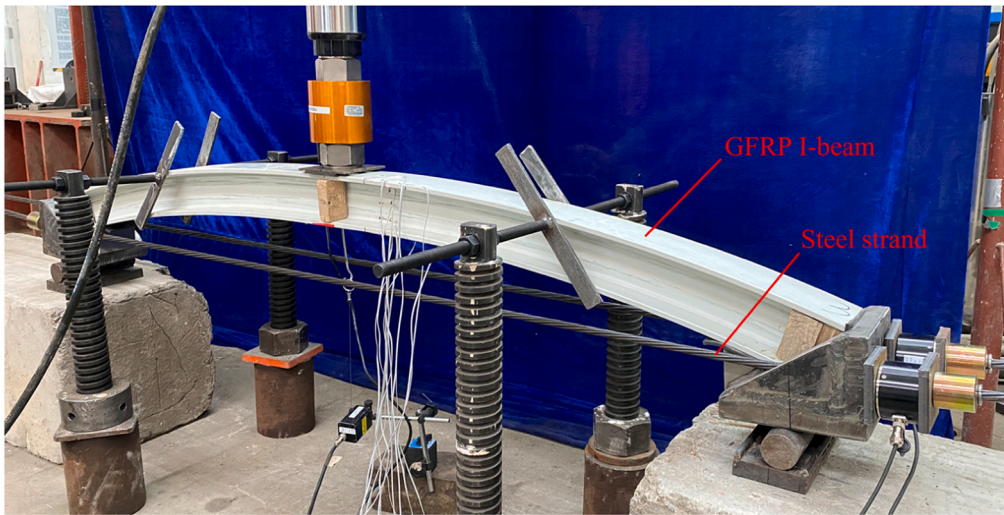
supported boundary condition. The average clear span of all beams is 1800 mm with variance of ± 20 mm, and the calculated arch rise is 162 mm with variance of ± 5 mm. The steel strand has diameter of 12.7 mm, elastic modulus of 195 GPa, ultimate tensile strength of 1860 MPa, and design tensile strength of 1320 MPa [33], and they were anchored at mid-height of beam end-sections. All tests were controlled within the design tensile strength of steel strands such that only the elastic behavior of steel strands was to be considered.

A hydraulic jack with maximum capacity of 500 kN was employed to apply the load in manner of displacement-control at rate of 2 mm/min. A steel bearing plate having thickness of 3.5 mm and a rubber plate having thickness of 5 mm were used to spread the point-load to the region of 75×100 mm (beam length \times width) to avoid possible stress concentration. The rubber plate was also used in between of GFRP arch beams and steel supports to avoid stress concentration. Moreover, wood stiffeners were used at mid- and end-sections, aiming to enhance the load-carrying capacity of beams subjected to concentrated loads. A linear variable differential transformer (LVDT) was installed at mid-span of beams to monitor the vertical displacement during the tests. Eight strain gages were installed near mid-span of six GFRP arch beams (i.e., three control specimens and three beam-string specimens) to measure the possible flange local buckling behavior and validate the plane section assumption. The layout of strain gages is illustrated in Fig. 4. Additionally, a pair of load transducers were installed at one end of all beam-string specimens to measure the actual tensile force in steel strands during tests. Two pairs of steel lateral supports were installed at third span of all specimens to prevent the possible lateral torsional buckling. In addition, the side plates of customized steel supports were also designed to prevent the beam-ends from possible lateral torsions. Thus, all beam specimens were exempt from out-of-plane deformations.

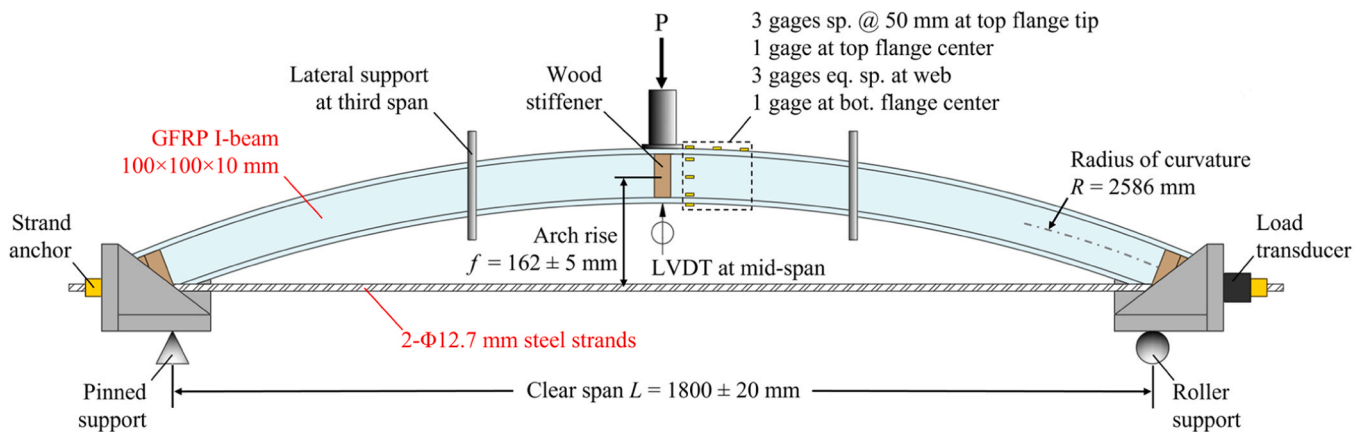
A total of four different boundary conditions were investigated in this work, and 12 specimens were categorized into four groups, with each group having three identical specimens for validating the repeatability of tests. Specifically, three control specimens were only subjected to simply-supported boundary conditions, and thus, they are denoted as specimens SS-1, -2, and -3. Three (out of nine) beam-string specimens were tested without pre-tensioning of steel strands such that their tension strings were relaxed before tests; these specimens are denoted as BS-relaxed-1, -2, and -3. In addition, another three beam-string specimens were tested with steel strands pre-tensioned to about 0% of their ultimate tensile strength to remove the relaxed part of tension strings; these specimens are denoted as BS-0%-1, -2, and -3. The last three beam-string specimens were tested with steel strands pre-tensioned to about 5% of their ultimate tensile strength, aiming to investigate the effect of pre-tensioning of tension strings on the flexural behavior of GFRP arch beam; these specimens are denoted as BS-5%-1, -2, and -3. All specimens were deemed failed (and tests were stopped) when sudden-catastrophic failure was occurred, and dramatic drop of load was observed.

2.3. Test results

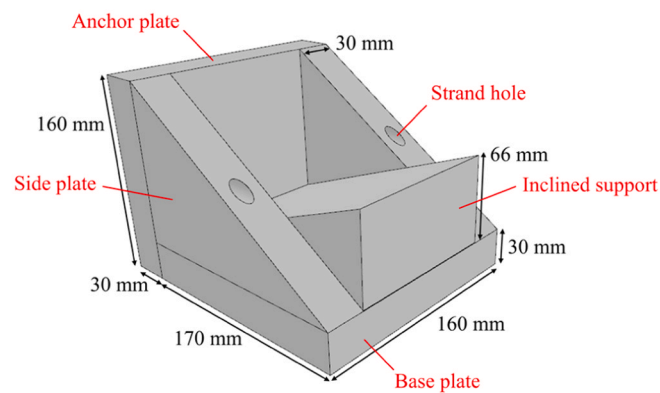
Experimentally-determined ultimate loads, maximum displacements, and linear stiffness of GFRP arch beams subjected to varying boundary conditions are presented in Table 2. It is noted that self-weight of GFRP arch beam, 56 N/m, is neglected in calculation of ultimate load, since its contribution to flexural strength of beam is less than 0.05% of observed value, and also, the stiffness is defined in form of strength-to-displacement ratio. From Table 2, it is seen that all the BS specimens exhibited higher flexural strength and stiffness as compared to SS counterparts; moreover, such an improvement in flexural performance tends to become more prominent with the increasing pre-tensioning in tension strings. Specimens BS-5% exhibited the highest flexural strength and stiffness, increased by 27% and 109%, respectively, as compared to control specimens; that is, with only 5% of pre-tensioning the proposed beam-string system is able to double the flexural stiffness of GFRP arch



(a) Overall view



(b) Schematic view



(c) Customized steel support

Fig. 3. Three-point bending test configuration.

beam.

Taking specimen BS-relaxed-1 as example, representative top flange and cross-sectional strains are shown in Fig. 4. From Fig. 4a, it is observed that all flange strains behaved almost in a linear-elastic

manner until failure; thus, flange local buckling is not of concern in this case, and the same behavior is also observed in all other specimens. From Fig. 4b, it is seen that strain distribution generally increased linearly with the sectional height; thus, plane section assumption can be

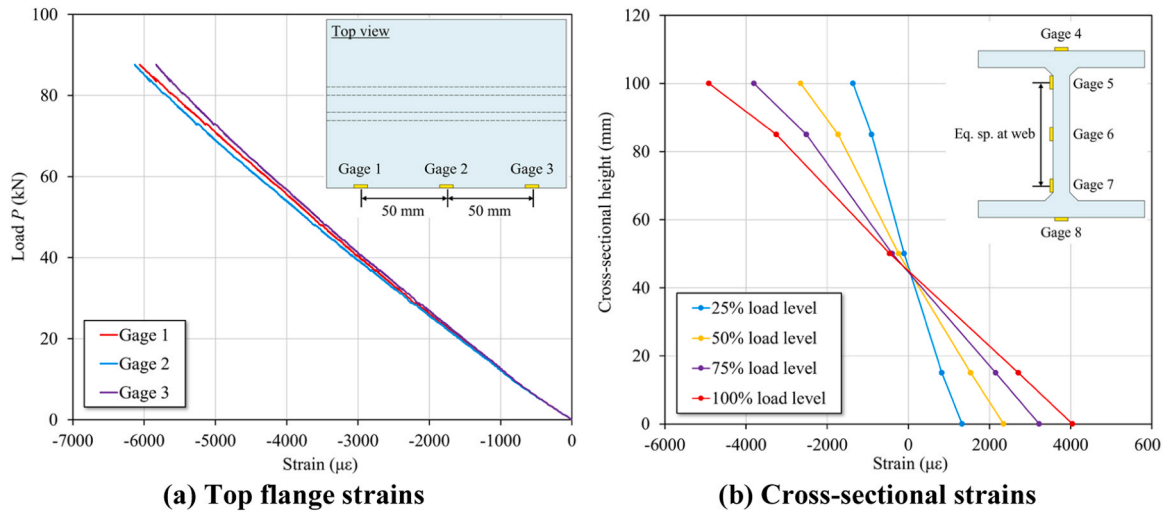


Fig. 4. Representative top flange and cross-sectional strains (BS-relaxed-1).

Table 2
Experimentally- and numerically-determined flexural performance of GFRP arch beams.

Specimens	Experimental results					Numerical results				
	Ultimate Load P (kN)	Avg. P (kN) (COV)	Max. displ. Δ (mm)	Linear stiffness K (kN/m)	Avg. K (kN/m) (COV)	Ultimate Load P (kN)	$\frac{P_{FEM}}{P_{exp}}$	Max. displ. Δ (mm)	Linear stiffness K (kN/m)	$\frac{K_{FEM}}{K_{exp}}$
SS-1	60.68 ^a	79.40 ^b	42.10	1462	1475	83.89	1.38 ^a	59.31	1436	0.98
SS-2	83.00	(-)	58.95	1481	(0.01)		1.01			0.97
SS-3	75.80		55.31	1468			1.11			0.98
BS-relaxed-1	88.58	88.12 ^b	44.40	2270	2176 (0.04)	89.40	1.01	44.47	2109	0.93
BS-relaxed-2	59.98 ^a		31.61	2233			1.49 ^a			0.94
BS-relaxed-3	87.65		44.09	2119			1.02			1.00
BS-0%-1	97.99	97.97	62.07	2070	2407	101.68	1.04	43.75	2496	1.21
BS-0%-2	100.55	(0.03)	54.00	2801	(0.18)		1.01			0.89
BS-0%-3	95.35		58.30	2012			1.07			1.24
BS-5%-1	100.36	100.56	37.21	3068	3079	104.32	1.04	31.17	2998	0.98
BS-5%-2	97.81	(0.03)	38.01	3036	(0.01)		1.07			0.99
BS-5%-3	103.52		34.61	3122			1.01			0.96

^a This is an outlier due to premature failure of specimen;
^b Outlier is not considered in calculation of the average load.

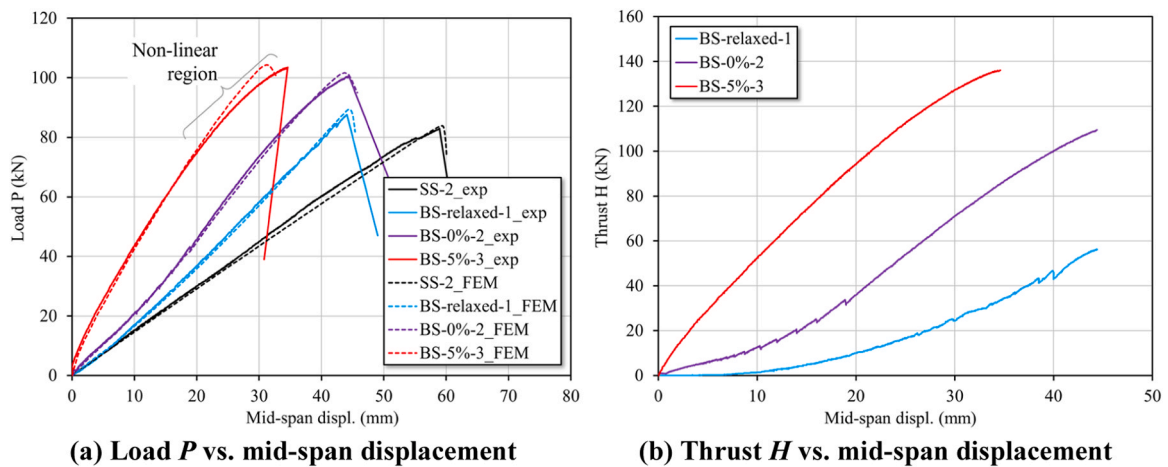


Fig. 5. Representative load-displacement and thrust-displacement curves.

validated.

Load-displacement and thrust-displacement curves of the four specimens having the highest loads from each type of boundary conditions are taken as the representatives, as shown in Fig. 5 (i.e., solid lines with subscripts of exp). From Fig. 5a, it is seen that BS-5%-3 exhibited the highest flexural strength and stiffness, followed by BS-0%-2, BS-relaxed-1, and SS-2. Moreover, the load-displacement curves of all specimens are observed, to noticeable extent, to show a slightly non-linear behavior. Such a non-linear behavior is susceptible attributed to the inherent geometric and material non-linearities of GFRP arch beam as well as the initial imperfections of test set-up.

The non-linear behavior is also evidenced by the measured tensile force of tension strings (i.e., thrust H in Fig. 5b). It is noted that the thrusts shown in Fig. 5b are the sum of two steel strands, and they are zeroed against their initial values before applying the load P . This is due to the fact that the possible camber of beams induced by pre-tensioning of strands was not restrained, and the resulting reaction at mid-span of beams was released. Thus, all beam-string specimens were self-balanced, and the structural behaviors of interests are those observed after applying the load P . With that said, the observed thrust of three BS specimens clearly show different behaviors. Initially-relaxed tension strings are seen not to take up the load until the GFRP arch beam experienced a vertical displacement almost 10 mm. With steel strands straightened (i.e., pre-tensioned to 0%), tension strings are able to take up the load simultaneously with deformation of GFRP arch beam; however, the load of tension strings is much lower than that pre-tensioned to 5%. Moreover, considering the widely-recognized linear-elastic behavior of steel strands, the observed thrusts indicate an imperfect load-transfer mechanism in the present configuration of beam-string system; that is, the measured thrusts (by load transducers at steel support) are susceptible to be affected by imperfections of test set-ups and the effective thrusts transferred to GFRP arch beams may be lower than measured values. The non-linear behavior of GFRP arch beams as well as the load-transfer mechanism between GFRP arch beams and steel strands are investigated in the following numerical program.

Taking specimen BS-relaxed-1 as example, typical failure modes of

GFRP arch beams are shown in Fig. 6. Additionally, failure modes of other types of specimens (i.e., SS, BS-0%, and BS-5%) are also provided, as shown in Fig. A.2. in Appendix A. Based on experimental observations, the first shear crack occurred at top flange-web junction under load point. With the loss of integrity of flange-web junction, web plate started to take over almost all the load and web crippling failure occurred near the load point, which is marked by tear-apart-like crack at web. Then, shear crack propagated along with the flange-web junction until reaching the end-sections of beam. All cracks occurred within an extremely short period, and the sound was similar to gunshot. These cracks are generally observed in all specimens, and they were not necessarily occurred following the same order for every specimen.

3. Numerical program

3.1. Finite element modeling

Finite element (FE) modeling was conducted via ABAQUS to simulate and validate the flexural behavior of curved-pultruded GFRP arch beams subjected to varying boundary conditions. Two types of models were constructed: the first one only modeling GFRP arch beam and the second one modeling both GFRP arch beam and steel strands, as shown in Fig. 7. The material properties were taken as those shown in Table 1. 2D shell element S4R was used to model the GFRP arch beam and 3D solid element C3D8R was used to model the steel strands. With mesh convergence tests, characteristic element sizes of 5.0 and 1.8 mm were respectively determined for shell and solid elements. All FE models were built mimicking the experimental set-ups, thus having simply-supported boundary condition and a concentrated displacement load at mid-span. In addition, the central surface region of 75×100 mm (beam length \times width) was coupled in all degrees of freedom with respect to the load point so as to simulate the effect of steel bearing plate. In the first FE model, horizontal thrust H was taken as the actual tensile forces measured from experimental tests (i.e., specimens BS-relaxed-1, BS-0%-2, and BS-5%-3) and it was applied at the roller-end of beam. In the second model, steel strands were constrained together with GFRP

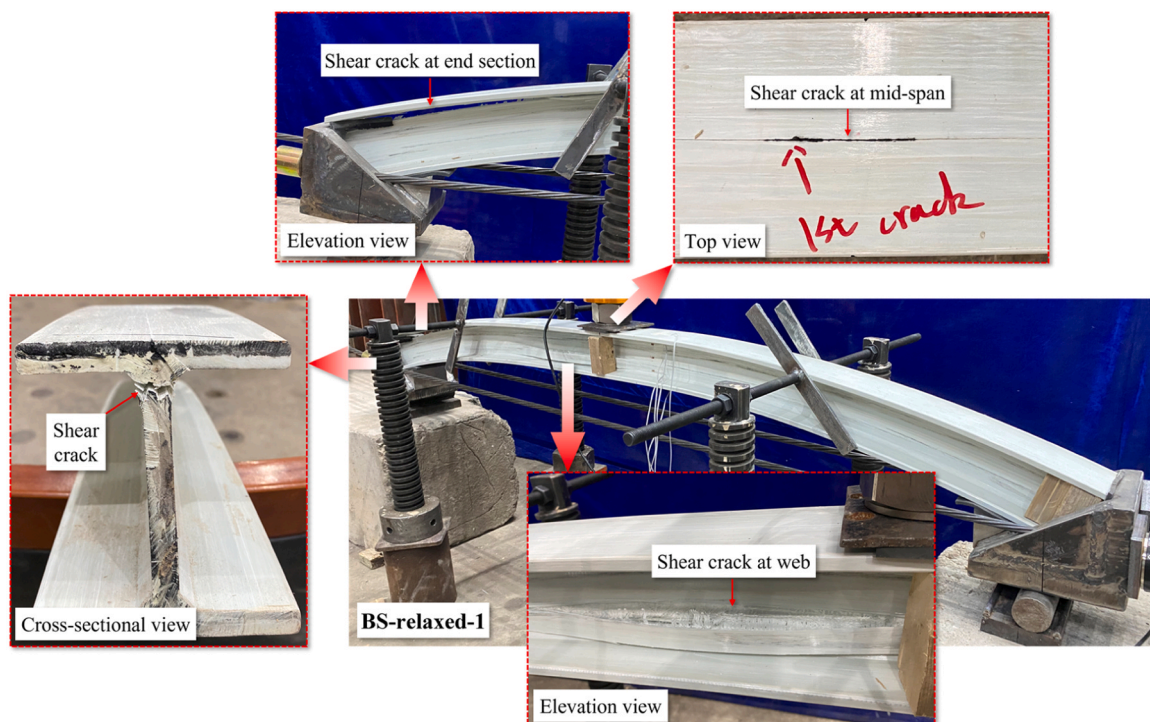


Fig. 6. Representative failure modes of GFRP arch beam (specimen BS-relaxed-1).

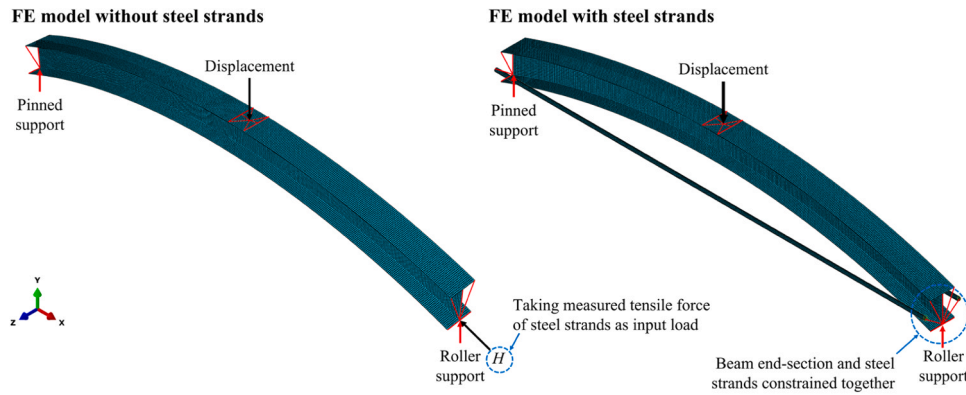


Fig. 7. Finite element models.

arch beam at both ends, thus permitting a perfect load-transfer mechanism. Comparing the two models, the first one is expected to yield a better agreement with experimental results since an imperfect load-transfer between GFRP arch beam and steel strands has been identified, and such an imperfect load-transfer can be observed by specimens BS-relaxed-1 and BS-0%–2 in Fig. 5b. Thus, the first model is focused in this section for validating the experimental results, meanwhile the second model is to validate the analytical results presented in next section.

In order to simulate the non-linear flexural behavior as well as identifying the failure/damage modes of GFRP arch beams, progressive failure was modeled in ABAQUS using Hashin damage criterion, which consist of three components, including damage initiation, damage evolution, and damage stabilization [34]. Damage initiation considers fiber- and matrix-dominated damages and determines the onset of four modes: 1) fiber tension; 2) fiber compression; 3) matrix tension; and 4) matrix compression [35,36], as expressed in Eqs. 1–4. Note that σ_{11} , σ_{22} , and σ_{12} are the three components of effective stress tensor σ , and α is the coefficient accounting for the contribution of shear stress to fiber tension damage mode. In addition, the longitudinal and transverse shear strength are approximately assumed to be equal to in-plane shear strength F_{LT} . Then, damage evolution is to reduce the stiffness of material based calculated damage variables, and in this process, the tensile and compressive fracture energies in fiber- and matrix-dominated directions must be specified so as to calculate the damage variables, including G_{ft} , G_{fc} , G_{mt} , and G_{mc} (subscripts f and m indicate fiber and matrix, and t and c indicate tensile and compressive) [37]. Last but not least, damage stabilization is to alleviate the convergence difficulties through four viscosity coefficients corresponding to tensile and compressive behavior in fiber- and matrix-dominated directions [37]. Detailed expressions regarding damage evolution and stabilization have been extensively addressed by previous studies (e.g., [36] and [37]), and therefore, they are not repeatedly discussed herein.

$$\text{Fiber tension : } \left(\frac{\sigma_{11}}{F_{LT}}\right)^2 + \alpha \left(\frac{\sigma_{12}}{F_{LT}}\right)^2 = 1, \sigma_{11} > 0 \quad (1)$$

$$\text{Fiber compression : } \left(\frac{\sigma_{11}}{F_{Lc}}\right)^2 = 1, \sigma_{11} < 0 \quad (2)$$

$$\text{Matrix tension : } \left(\frac{\sigma_{22}}{F_{Tt}}\right)^2 + \left(\frac{\sigma_{12}}{F_{LT}}\right)^2 = 1 \quad (3)$$

$$\text{Matrix compression : } \left(\frac{\sigma_{22}}{2F_{LT}}\right)^2 + \left[\left(\frac{F_{Tc}}{2F_{LT}}\right)^2 - 1\right] \frac{\sigma_{22}}{F_{Tc}} + \left(\frac{\sigma_{12}}{F_{LT}}\right)^2 = 1 \quad (4)$$

Representative data of fracture energies and viscosity coefficients available in literature are summarized in Table 3. The present work empirically adopted the highest fracture energies pertaining to fiber from literature (i.e., $G_{ft} = G_{fc} = 100$ N/mm) and proposed a new set of

Table 3
Fracture energies and viscosity coefficients in literature and present work.

Authors	Materials ^a	G_{ft} (N/mm)	G_{fc} (N/mm)	G_{mt} (N/mm)	G_{mc} (N/mm)	Viscosity coefficients η
Lapczyk and Hurtado [37]	GF/EP	12.5	12.5	1.0	1.0	$\eta_f = 0.00025$; $\eta_m = 0.005^b$
Sharma et al. [38]	GF/EP	92	79	0.22	0.61	-
Tarfaoui et al. [39]	CF/EP	100	100	5	5	0.001
Alhawamdeh et al. [34, 40]	GF/VE	92	79	5	5	0.001
Present work	GF/EP	100	100	14	14	0.001; 0.0035; 0.0025

^a GF indicates glass fiber; CF indicates carbon fiber; EP indicates epoxy resin; VE indicates vinyl ester resin;

^b Viscosity coefficients η_f and η_m are for fiber and matrix, respectively.

fracture energies for matrix based on regression of current experimental data (i.e., $G_{mt} = G_{mc} = 14$ N/mm). It is noted that experimental tests are required to obtain an accurate characterization of fracture energies of pGFRP profiles, while in this work such type of tests is not conducted. The selected fracture energies are seen to achieve satisfactory accuracy; that is, those data, though empirically determined, are able to provide a general characterization of the properties as well as the imperfections of the material. In addition, viscosity coefficients η are generally obtained through data-fitting process based on experimental results [34,37–40]. Thus, the same method with previous studies was adopted, and in this work, $\eta = 0.001$ for specimens SS and BS-relaxed; $\eta = 0.0035$ for specimen BS-0%; $\eta = 0.0025$ for specimen BS-5%. Taking specimen SS-2 as example, the effects of fracture energies and viscosity coefficients are illustrated in Fig. 8a. In general, the fracture energies and viscosity coefficients adopted in this work are in similar region with existing data.

In addition to progressive failure of GFRP material, the load-transfer mechanism between GFRP arch beam and steel strands was investigated. In the tests, the horizontal thrust to GFRP arch beam was realized through a pair of customized steel supports in between of the beam and steel strands. Although the force of strands was measured, a certain extent of loss might exist due to the imperfect transfer of load. Through a parametric study, 20%, 30%, and 15% reductions of recorded forces were identified for specimens BS-relaxed-1, BS-0%–2, and BS-5%–3, respectively. Taking specimen BS-5%–3 as example, the effects of viscosity coefficients and effective thrusts are illustrated in Fig. 8b.

With the progressive failure-related parameters and the losses of thrusts determined, numerically-determined flexural strength and stiffness are obtained, as shown in Table 2. The load-displacement curves of

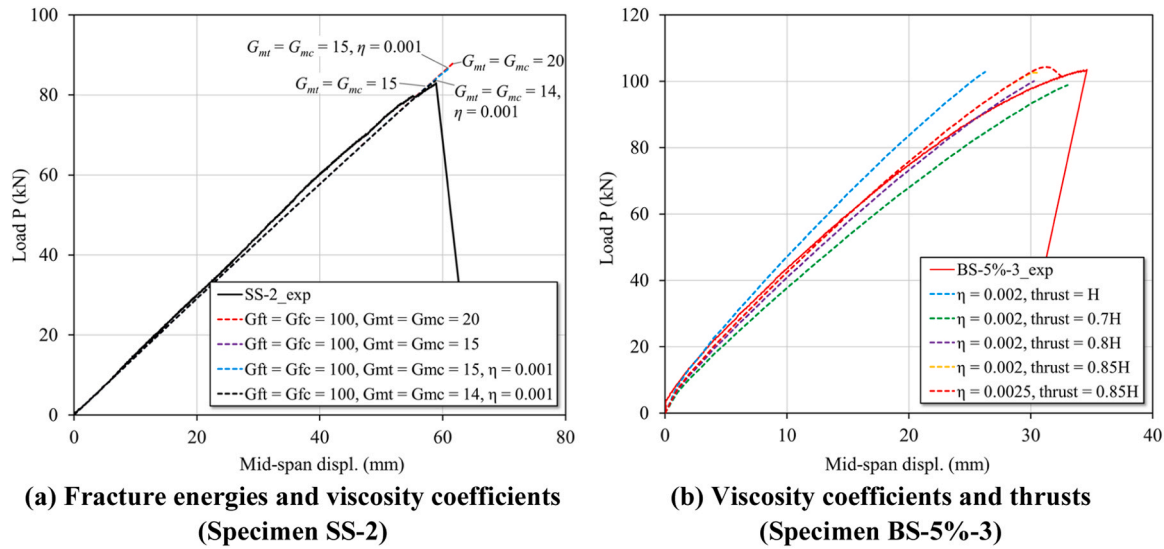


Fig. 8. Parametric study on fracture energies, viscosity coefficients, and effective thrusts.

four representative specimens are also obtained, as shown in Fig. 5a. In general, FE modeling could satisfactorily predict both the flexural strength and stiffness for GFRP arch beams subjected to varying boundary conditions. For flexural strength, the average ratio of FE modeling and test results is 1.04, with COV of 0.03; and for flexural stiffness, the average ratio of FE modeling and test results is 1.01, with COV of 0.11.

3.2. Failure modes

Using Hashin damage criterion, typical failure/damage modes of GFRP arch beams were simulated, as shown in Fig. 9. In particular, the field outputs DAMAGESHR (i.e., shear damage) and HSNMTCRT (i.e., matrix tension damage) were taken as the main criteria for identifying failure modes, as these two variables directly account for overall shear damage of material and transverse tensile damage of matrix (see Eq. 3). This method has been successfully demonstrated by Alhawamdeh et al. [34,40]. From Fig. 9a, it can be seen that in general, the main failure mode of GFRP arch beam includes the shear damage and matrix tensile damage at top flange-web junction, with the latter being developed into the web. Specifically, in the tests almost all GFRP arch beams are found to start cracking at top flange-web junction near the load point, and this type of failure mode can be accurately simulated by FE modeling, as shown by shear failure in Fig. 9b. Moreover, when flange-web junction loses its integrity, web plate is to take over the load and web crippling failure may occur. This type of failure mode is seen to be similar to tear-apart-like crack, as illustrated by matrix tension damage at web in Fig. 9c. In conclusion, Hashin damage criterion is observed to provide accurate predictions of failure modes for GFRP arch beams addressed in this work.

4. Analytical program

4.1. Flexural strength of GFRP arch beam

Failure mode of all GFRP arch beams is observed to be controlled by shear damage at top flange-web junction and/or web plate. This type of failure mode is characterized as the web crippling of structural members subjected to concentrated loads by ASCE Pre-standard [41]. Web crippling behavior has been investigated by many researchers, including Borowicz and Bank [42], Wu and Bai [43], Wu et al. [44], Fernandes et al. [45,46], and Haloi et al. [47]. The main difference between previous studies lies in the test configuration and observed failure modes.

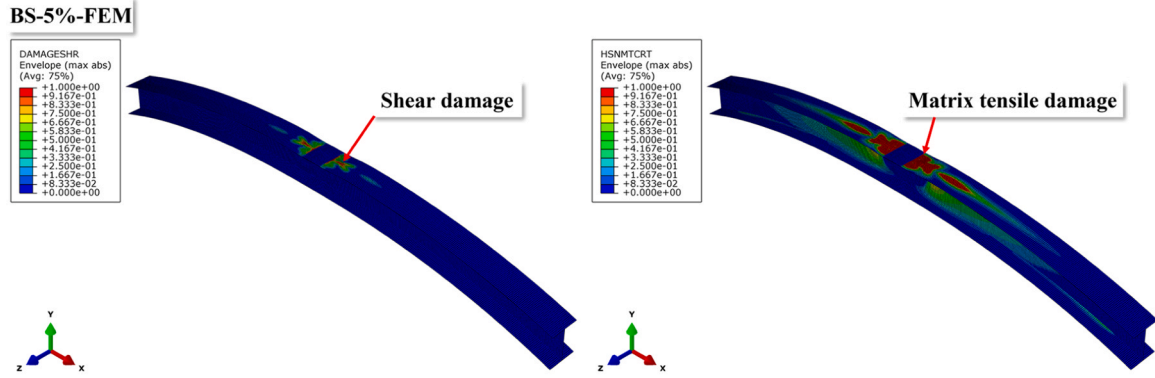
Three-point bending tests on short beams was conducted by Borowicz and Bank [42], while other tests were carried out on pGFRP profiles only subjected to compressive loads. Due to the varying slenderness ratios of web plates being addressed in those tests, three types of failure modes are identified, including through-web shear damage [42], localized junction shear damage [43], and web buckling [45], as shown in Fig. 10. Accordingly, different predictive models are developed with respect to each failure mode. In this work, the flexural test set-up is similar to which Eq. 5 was based off, and through-web shear damage is found to be the dominant failure mode for GFRP arch beams, as shown in Fig. 10d. Thus, the predictive model proposed by Borowicz and Bank [42] is adopted to calculate the web crippling strength, as shown in Eq. 5.

$$P_n = 0.7d t_w F_{ILS} \left(1 + \frac{2k + 6t_{plate} + b_{plate}}{d} \right) \quad (5)$$

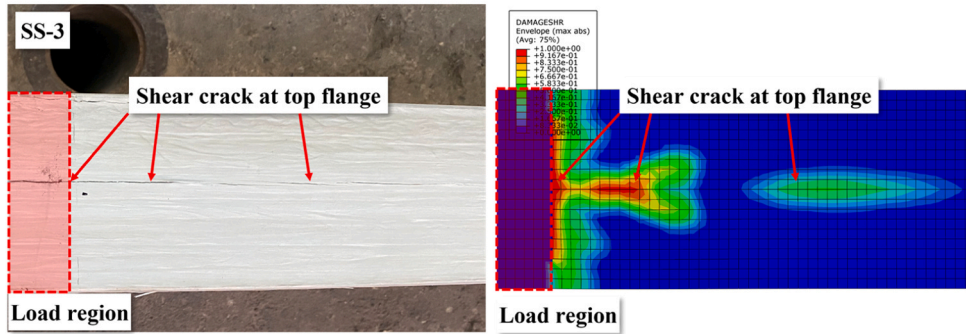
Where d is the section depth; t_w is the web thickness; F_{ILS} is the inter-laminar shear strength of material, approximately taken as in-plane shear strength F_{LT} in this case; k is the distance from top of beam to bottom of fillet, measured as 15 mm in this case; t_{plate} and b_{plate} are the thickness and length of bearing plate, respectively measured as 3.5 and 75 mm in this case. It is noted that ASCE adopted Eq. 5 with a conservative modification, namely replacing d with d_w in the second term in parentheses, and d_w is the depth of web plate. The term of $0.7d$ is to simulate the crack length at web, while in this work, it is measured as $0.65\text{--}0.68d$, as shown in Fig. 10d. Thus, $0.65d$ is used for conservative purpose. Despite of having actual failure mode respected, Eq. 5 is found to over-estimate the web crippling strength observed in this work, by a factor about 1.34. This is mainly due to the non-uniform shear distribution across web plate (in height direction). From FE modeling, it is found that the average shear stress over $0.65d$ region of web plate is about 61 MPa, which is 72% of shear strength of material, as shown in Fig. 11. Thus, Eq. 5 is modified, as shown in Eq. 6.

$$P_n = 0.65d t_w (c F_{ILS}) \left(1 + \frac{2k + 6t_{plate} + b_{plate}}{d} \right) \quad (6)$$

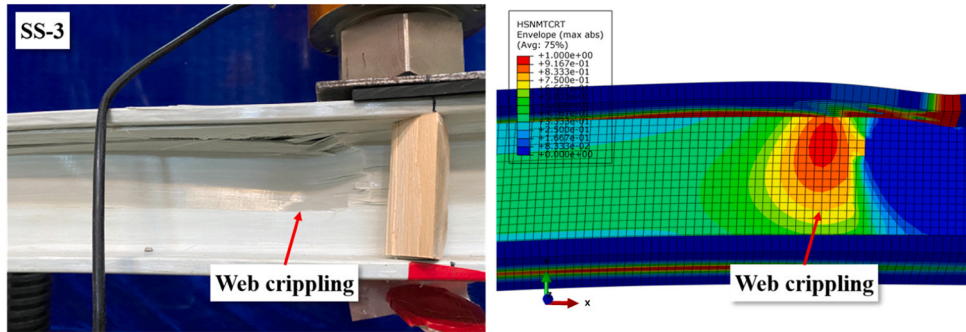
Where c is the coefficient accounting for non-uniform shear distribution across crack region of web plate, taken as 0.72 in this case; and $0.65d$ is the crack length. The predicted web crippling strength, namely flexural strength of GFRP arch beam in this work, is shown in Table 4. Excluding the two outliers (i.e., SS-1 and BS-relaxed-2), the average ratio of analytical predictions and experimental results is 0.97, with COV of 0.10. Additionally, for all beam-strings with pre-tensioned strings (i.e.,



(a) Failure modes of GFRP arch beam (overall view)



(b) Top flange failure (top view)



(c) Web failure (elevation view)

Fig. 9. Typical failure modes simulated by FE modeling.

six specimens of BS-0% and BS-5%), Eq. 6 could uniformly provide conservative predictions, with average ratio of 0.90 and COV of 0.03. Thus, good accuracy of Eq. 6 can be demonstrated.

4.2. Internal forces of GFRP beam-string

In this section, the internal forces of GFRP beam-string are calculated, including internal moment M , shear force Q , and axial force N . To do so, the horizontal thrust H must be solved first. GFRP beam-string is a first-degree indeterminate structure, and the force method can be implemented. The steel strands are replaced with a pair of horizontal forces H , and the free body diagram of GFRP beam-string is obtained, as shown in Fig. 12. The compatibility condition regarding deformation is given in Eq. 7.

$$\delta_{11}H + \Delta_{1P} = 0 \quad (7)$$

Where P is the external load; H is the horizontal force of two steel strands; δ_{11} and Δ_{1P} are the displacements generated by horizontal force H and vertical load P , respectively, and they are calculated through Eqs.

8 and 9. In this case, the displacement due to internal shear force of beam is neglected.

$$\delta_{11} = \int \frac{\bar{M}_1^2}{E_L I_{beam}} ds + \int \frac{\bar{N}_1^2}{E_L A_{beam}} ds + \frac{L}{E_s A_s} \quad (8)$$

$$\Delta_{1P} = \int \frac{\bar{M}_1 M_P}{E_L I_{beam}} ds \quad (9)$$

Where E_L is the longitudinal modulus of GFRP; I_{beam} is the moment of inertia of GFRP arch beam; A_{beam} is the cross-sectional area of GFRP arch beam; E_s is the elastic modulus of steel strand; A_s is the cross-sectional area of two steel strands; M_P is the moment at mid-span generated by external load P ; \bar{M}_1 is the moment at mid-span generated by a virtual unit load in the direction of H ; and \bar{N}_1 is the axial force at mid-span generated by a virtual unit load in the direction of H . \bar{M}_1 and \bar{N}_1 are given as:

$$\bar{M}_1 = -y \quad (10)$$

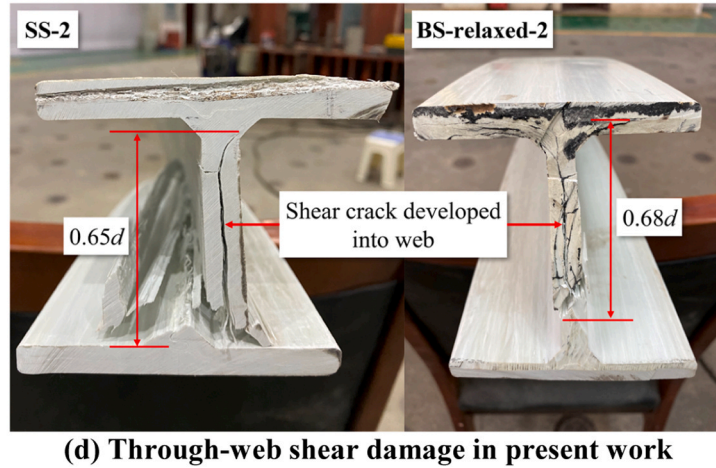
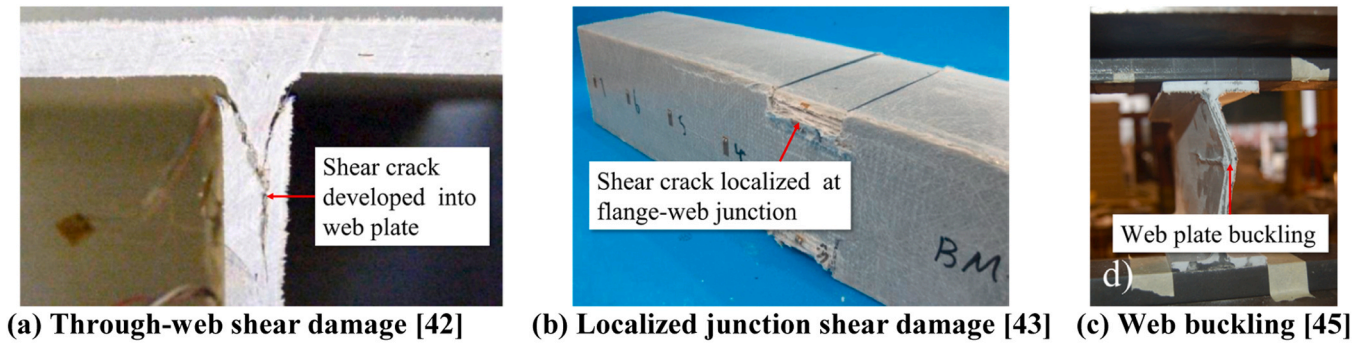


Fig. 10. Typical failure modes of web crippling in literature and present work.

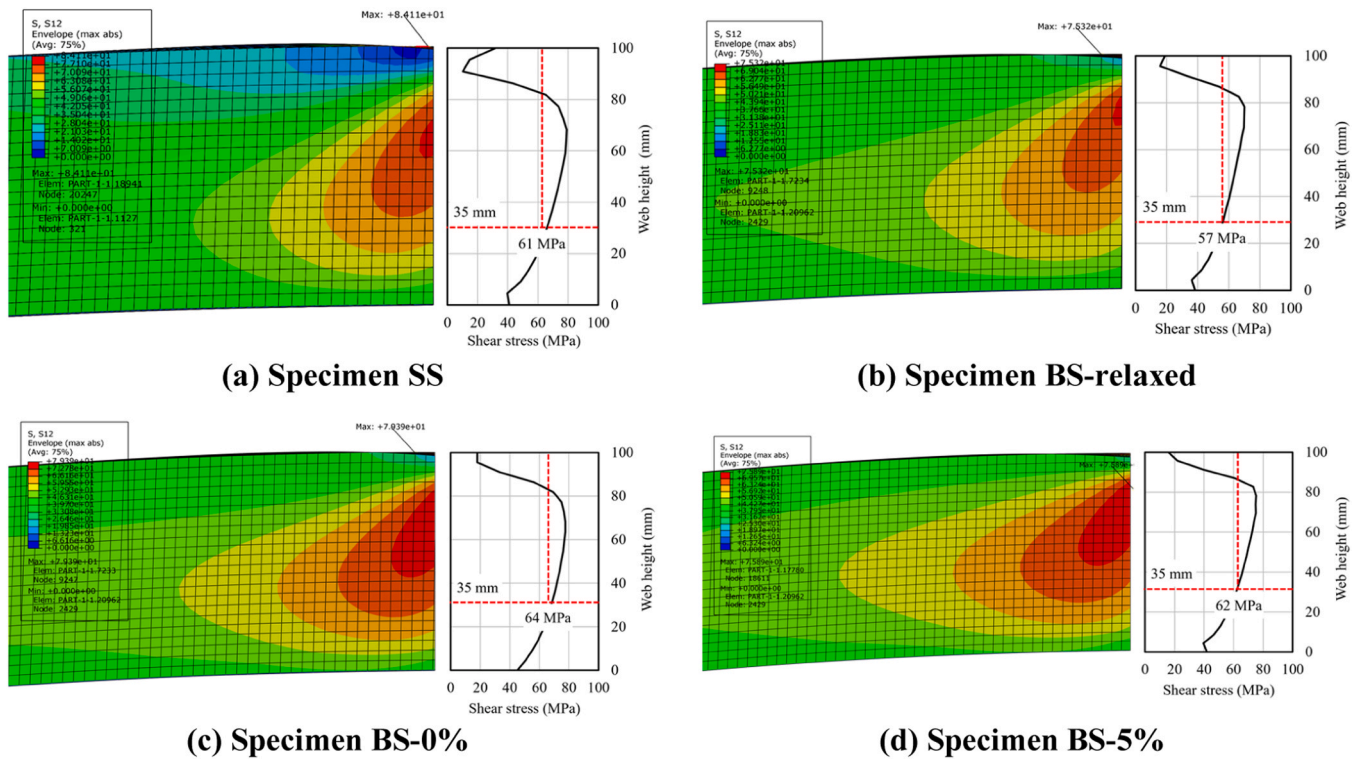


Fig. 11. Non-uniform shear distribution across web plate.

Table 4
Comparison between analytically- and experimentally-determined web crippling strength.

Specimens	Experimental results	Analytical predictions	
	P_{exp} (kN)	P_{pred} (kN)	$\frac{P_{pred}}{P_{exp}}$
SS-1	60.68 ^a	89.18	1.47 ^a
SS-2	83.00		1.07
SS-3	75.80		1.18
BS-relaxed-1	88.58		1.01
BS-relaxed-2	59.98 ^a		1.49 ^a
BS-relaxed-3	87.65		1.02
BS-0%-1	97.99		0.91
BS-0%-2	100.55		0.89
BS-0%-3	95.35		0.94
BS-5%-1	100.36		0.89
BS-5%-2	97.81		0.91
BS-5%-3	103.52		0.86

^a This is an outlier due to premature failure of specimen.

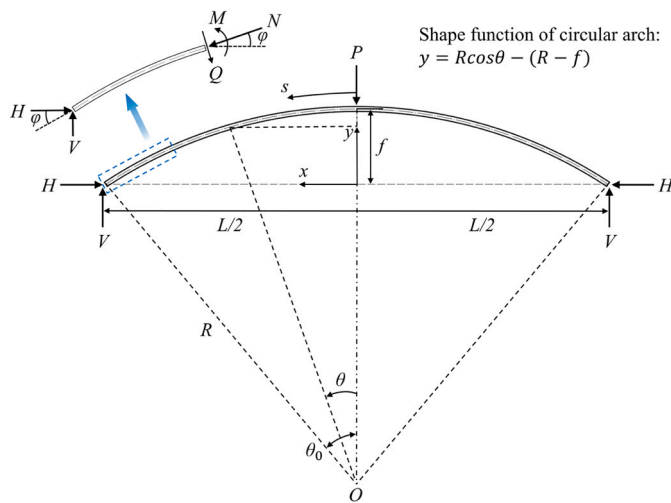


Fig. 12. Free body diagrams of GFRP arch beam (polar coordinate system).

$$\bar{N}_1 = \cos \varphi \quad (11)$$

Where φ is the cross-sectional angle, which is calculated taking the first derivative of shape function y . Then, substituting Eqs. 8–11 into Eq. 7, and taking $ds = R d\theta$, yields:

$$H = \frac{2 \int_0^{\theta_0} \frac{y M_P}{E_L I_{beam}} R d\theta}{2 \int_0^{\theta_0} \frac{y^2}{E_L I_{beam}} R d\theta + 2 \int_0^{\theta_0} \frac{\cos^2 \varphi}{E_L A_{beam}} R d\theta + \frac{L}{E_s A_s}} \quad (12)$$

With the horizontal force H of steel strands determined, the internal forces of GFRP beam-string can be calculated using Eqs. 13–15.

$$M = M_{ss} - Hy \quad (13)$$

$$Q = Q_{ss} \cos \varphi - H \sin \varphi \quad (14)$$

$$N = Q_{ss} \sin \varphi + H \cos \varphi \quad (15)$$

Where M_{ss} and Q_{ss} are the internal moment and shear force of simply-supported GFRP beam; and φ is the cross-sectional angle of GFRP beam. At mid-span (i.e., $\varphi = 0^\circ$), the shear force Q of GFRP beam-string is equal to the shear force Q_{ss} of its simply-supported counterpart; and

the axial force N is equal to the horizontal force H .

The second FE model with steel strands (see Fig. 7) is used to validate the analytically predicted horizontal thrust H , as shown in Fig. 13a. Through the load-displacement curves in Fig. 13a, it is seen that the BS model with steel strands has the highest flexural stiffness and behaves in perfectly linear-elastic manner, though its flexure strength is lower than the first model (i.e., BS-5%–3_FEM). The lower strength of second FE model is due to the fact that the progressive failure is not considered. The numerically-predicted ultimate load is 92.91 kN. Taking this value as input for analytical model, horizontal thrust can be calculated, which is 155.92 kN. The difference between analytically- and numerically-predicted thrusts is only about 1.67%, showing an excellent accuracy of analytical model. Then, using this thrust, the internal forces of beam-string (i.e., moment M , shear force Q , and axial force N) can be calculated, as shown in Figs. 13b, 13c, and 13d. The solid lines represent the beam-string structure, and dashed lines represent the simply-supported counterpart. It is seen that beam-string is able to decrease the internal moment due to the enabled arch mechanism, and the internal shear can also be generally reduced while the maximum shear remains the same. For any given external load P , analytically-predicted internal forces of beam-string shall be higher than the actual forces, since the load-transfer mechanism between GFRP arch beam and steel strands is inevitably imperfect for the present structural configuration. Higher internal forces are to result in a conservative design, which is acceptable in practice.

5. Discussions

First, proposed beam-string system is demonstrated to be able to improve the flexural stiffness of GFRP arch beam, by up to 109%. Nonetheless, it is observed that the load-transfer between GFRP arch beam and steel strands is inevitably imperfect. The average loss of thrusts is found to be about 22%. This partially explains the lower flexural stiffness of all beam-strings as compared to the “perfect” FE model (i.e., the second model with steel strands). Although imperfect contacts between components are inevitable, the flexural stiffness of GFRP beam-string is believed to be improved provided the thrust is applied to GFRP arch beam through a more efficient method, and this method must allow the pre-tensioning of tension strings. Thus, future work is needed to develop a new beam-string configuration to achieve a higher efficiency in terms of load-transfer.

Second, varying extent of non-linear-elastic behaviors are observed in GFRP arch beams. Typically, non-linear behavior is attributed to the non-linear geometry of structure and/or non-linear nature of material. The linear load-displacement curve of the “perfect” FE model (i.e., the second FE model with steel strands) successfully demonstrates that the circular geometry of GFRP arch beam is not the main reason for observed non-linear behavior. With that said, it can be concluded that the progressive failure of GFRP material caused the non-linear behavior. Hashin damage criterion with damage evolution and stabilization is found to be able to provide accurate predictions regarding the non-linear flexural behavior of GFRP arch beams. The fracture energies and viscosity coefficients reported in this work could be potentially used to predict the progressive failure of similar materials and structures, meanwhile experimental tests are recommended to be conducted in future work so as to obtain an accurate characterization of fracture energies and viscosity coefficients.

Third, curved-pultruded GFRP arch beams addressed in this work are seen to be controlled by web crippling strength, rather than flexural strength of material. This behavior is similar to conventional pGFRP flexural members subjected to concentrated loads. Indeed, pGFRP members typically tend to fail due to concentrated loads. The horizontal thrusts (and the resulting axial forces) are observed to improve the web crippling strength, by up to 27%. Existing model for web crippling does not consider the arch mechanism of pGFRP members; that is, the effect of horizontal thrust on web crippling remains unknown. In future work, it is recommended to address the effect of interlaminar shear coupled

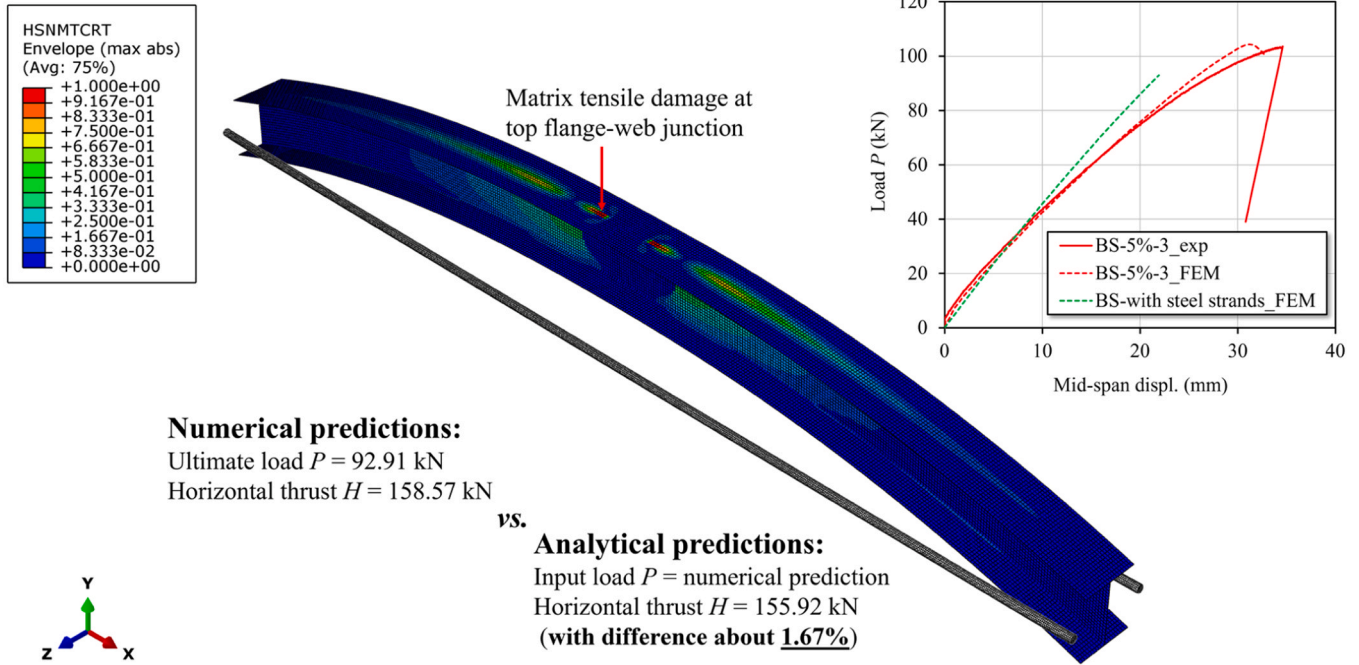
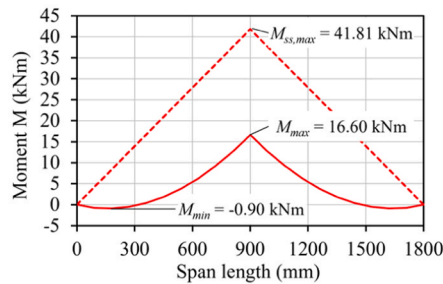
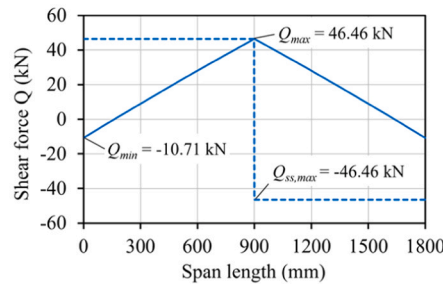
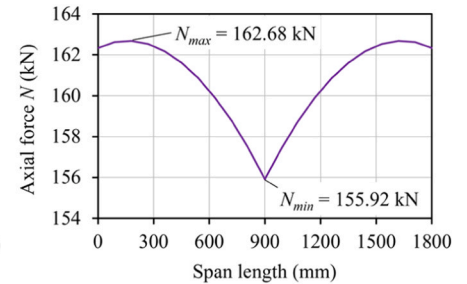
(a) FE model with steel strands**(b) Moment vs. span length****(c) Shear force vs. span length****(d) Axial force vs. span length**

Fig. 13. Comparison of numerical and analytical predictions.

with axial load on web crippling behavior of pGFRP members.

Last but not least, flexural performance of GFRP beam-string is highly dependent on the axial stiffness of tension strings. In this work, a pair of steel strands having diameter of 12.7 mm is adopted and three types of boundary conditions are investigated, including initially-relaxed string (i.e., BS-relaxed), initially-straightened strings (i.e., BS-0%), and pre-tensioned strings (i.e., BS-5%). A small pre-tensioning of 5% could lead to greatly improved flexural stiffness of GFRP arch beam. Thus, it can be readily expected that greater flexural stiffness of GFRP beam-string can be achieved provided a new tension string with higher axial stiffness and/or higher pre-tensioning. Again, the design of tension string shall be incorporated into the design of beam-string configuration. An efficient beam-string configuration with stronger tension string could rationally yield an improved flexural performance of GFRP beam-string.

6. Conclusions

In this work, flexural performance of curved-pultruded GFRP arch beams subjected to varying boundary conditions was investigated through experimental, numerical, and analytical programs. It is observed that the flexural strength and stiffness of GFRP arch beams was successfully enhanced by up to 27% and 109%, respectively. The improved flexural performance was attributed to the arch mechanism enabled by proposed GFRP beam-string structure. In addition, the progressive failure of GFRP material and the imperfect load-transfer

between GFRP arch beam and tension string were investigated through finite element modeling. Hashin damage criterion was developed based on experimental data obtained in this work as well as those available in literature, and 22% loss of thrusts (by average) were found in present beam-string configuration. Then, web crippling strength of GFRP arch beams was predicted with modifications to an existing model, and improved accuracy was observed. In addition, internal forces of beam-string were calculated. In future work, it is recommended to develop a new beam-string configuration so as to achieve a higher load-transfer efficiency as well as a higher flexural stiffness.

The GFRP beam-string structure proposed in this work is aimed to shed light on possible approach to improve the flexural stiffness of pGFRP members. Based on the successful demonstration of this work, possible applications of curved-pultruded GFRP members can be greatly broadened, such as the long-span spatial roof structures and heavy-duty vehicle bridges.

CRediT authorship contribution statement

TianQiao Liu: Conceptualization, Formal analysis, Funding acquisition, Investigation, Methodology, Project administration, Software, Visualization, Writing – original draft. **Peng Feng:** Conceptualization, Funding acquisition, Methodology, Project administration, Writing – review & editing. **Yulei Bai:** Writing – review & editing, Methodology. **Shangcong Bai:** Investigation, Methodology. **Jia-Qi Yang:**

Methodology, Writing – review & editing. **Fei Zhao:** Funding acquisition, Methodology, Writing – review & editing.

Declaration of Competing Interest

The authors declare that they have no known competing financial interests or personal relationships that could have appeared to influence the work reported in this paper.

Data Availability

Data will be made available on request.

Acknowledgements

This work was supported by National Key R&D Program of China (2023YFB3711600), National Natural Science Foundation of China (51908321), Nonmetallic Excellence and Innovation Center for Building Materials (2022TDA1-1), Chongqing Construction Science and Technology Plan Project (ChengKeZi2022No.2-1), and Natural Science Foundation of Hainan Province (520RC549).

Appendix A. Supporting information

Supplementary data associated with this article can be found in the online version at [doi:10.1016/j.engstruct.2024.117962](https://doi.org/10.1016/j.engstruct.2024.117962).

References

- Hollaway LC. A review of the present and future utilisation of FRP composites in the civil infrastructure with reference to their important in-service properties. *Constr Build Mater* 2010;24(12):2419–45.
- Cromwell JR, Harries KA, Shahrooz BM. Environmental durability of externally bonded FRP materials intended for repair of concrete structures. *Constr Build Mater* 2011;25(5):2528–39.
- Vedernikov A, Safonov A, Tucci F, Carlone P, Akhatov I. Pultruded materials and structures: A review. *J Compos Mater* 2020;0021998320922894.
- Zou X, Feng P, Bao Y, Wang J, Xin H. Experimental and analytical studies on shear behaviors of FRP-concrete composite section. *Eng Struct* 2020;215:110749.
- Alajarmeh O, Zeng X, Aravinthan T, Shelley T, Alhawamdeh M, Mohammed A, et al. Compressive behaviour of hollow box pultruded FRP columns with continuous-wound fibres. *Thin-Walled Struct* 2021;168:108300.
- Liu TQ, Liu X, Feng P. A Comprehensive Review on Mechanical Properties of Pultruded FRP Composites Subjected to Long-Term Environmental Effects. *Compos Part B: Eng* 2020;191:107958.
- Yang JQ, Feng P. Analysis-oriented models for FRP-confined concrete: 3D interpretation and general methodology. *Eng Struct* 2020;216:110749.
- Hu L, Feng P. Prestressed CFRP-reinforced steel columns under axial and eccentric compression. *Compos Struct* 2021;268:113940.
- Feng P, Wu Y, Ding Y, Liu T, Tian Y. Quasi-plastic flexural behavior of adhesive-bolt hybrid connection for large scale pultruded GFRP frame. *Eng Struct* 2021;238:112200.
- Liu, T.Q. (2017). Stability behavior of pultruded glass-fiber reinforced polymer I-sections subject to flexure (Doctoral dissertation, University of Pittsburgh).
- Kollár LP. Local buckling of fiber reinforced plastic composite structural members with open and closed cross sections. *ASCE. J Struct Eng* 2003;129(11):1503–13.
- Tarján G, Sapkás A, Kollár LP. Stability analysis of long composite plates with restrained edges subjected to shear and linearly varying loads. *J Reinf Plast Compos* 2010;29(9):1386–98.
- Nguyen TT, Chan TM, Mottram JT. Lateral-torsional buckling resistance by testing for pultruded FRP beams under different loading and displacement boundary conditions. *Compos Part B: Eng* 2014;60:306–18.
- Liu TQ, Harries KA. Flange local buckling of pultruded GFRP box beams. *Compos Struct* 2018;189:463–72.
- Liu TQ, Vieira JD, Harries KA. Lateral torsional buckling and section distortion of pultruded GFRP I-sections subject to flexure. *Compos Struct* 2019;225:111151.
- Liu TQ, Vieira JD, Harries KA. Predicting Flange Local Buckling Capacity of Pultruded GFRP I-Sections Subject to Flexure. *J Compos Constr* 2020;24(4):04020025.
- Yang JQ, Liu TQ, Feng P. Enhancing Flange Local Buckling Strength of Pultruded GFRP Open-Section Beams. *Compos Struct* 2020;244:112313.
- Liu TQ, Feng P, Lu X, Yang JQ, Wu Y. Flexural Behavior of Novel Hybrid Multicell GFRP-Concrete Beam. *Compos Struct* 2020;250:112606.
- Deskovic N, Triantafyllou TC, Meier U. Innovative Design of FRP Combined with Concrete: Short-Term Behavior. *J Struct Eng* 1995;121(7):1069–78.
- Correia JR, Branco FA, Ferreira JG. Flexural behaviour of multi-span GFRP-concrete hybrid beams. *Eng Struct* 2009;31(7):1369–81.
- Fam A, Honickman H. Built-up hybrid composite box girders fabricated and tested in flexure. *Eng Struct* 2010;32(4):1028–37.
- Gemi L, Madenci E, Özkılıç YO. Experimental, analytical and numerical investigation of pultruded GFRP composite beams infilled with hybrid FRP reinforced concrete. *Eng Struct* 2021;244:112790.
- Chen J, Zhu Y, Wang F, Feng B. Experimental and analytical study of hollow section concrete-filled GFRP tubes in bending. *Thin-Walled Struct* 2022;177:109297.
- Li S, Chan TM, Young B. Behavior of GFRP-concrete double tube composite columns. *Thin-Walled Struct* 2022;178:109490.
- Liu TQ, Feng P, Wu Y, Liao S, Meng X. Developing an innovative curved-pultruded large-scale GFRP arch beam. *Compos Struct* 2021;256:113111.
- Zhang J, Zhou P, Guan C, Liu TQ, Kang WH, Feng P, et al. An ultra-lightweight CFRP beam-string structure. *Compos Struct* 2021;257:113149.
- ASTM D3039. Standard Test Method for Tensile Properties of Polymer Matrix Composite Materials. West Conshohocken, PA: ASTM International; 2017.
- ASTM D6641. Standard Test Method for Compressive Properties of Polymer Matrix Composite Materials Using a Combined Loading Compression (CLC) Test Fixture. West Conshohocken, PA: ASTM International; 2014.
- ASTM D5379. Standard Test Method for Shear Properties of Composite Materials by the V-Notched Beam Method. West Conshohocken, PA: ASTM International; 2012.
- ASTM D7264. Standard Test Method for Flexural Properties of Polymer Matrix Composite Materials. West Conshohocken, PA: ASTM International; 2015.
- ASTM D2584. Standard Test Method for Ignition Loss of Cured Reinforced Resins. West Conshohocken, PA: ASTM International; 2011.
- ASTM D638. Standard Test Method for Tensile Properties of Plastics. West Conshohocken, PA: ASTM International; 2014.
- GB 50010. (2010). Code for Design of Concrete Structures. Ministry of Housing and Urban-Rural Construction of the People's Republic of China General Administration of Quality Supervision, Inspection and Quarantine of the People's Republic of China.
- Alhawamdeh M, Alajarmeh O, Aravinthan T, Shelley T, Schubel P, Kemp M, et al. Modelling hollow pultruded FRP profiles under axial compression: Local buckling and progressive failure. *Compos Struct* 2021;262:113650.
- Hashin Z, Rotem A. A fatigue failure criterion for fiber reinforced materials. *J Compos Mater* 1973;7(4):448–64.
- Hashin Z. Failure criteria for unidirectional fiber composites. *J Appl Mech* 1980;47:329–34.
- Lapczyk I, Hurtado JA. Progressive damage modeling in fiber-reinforced materials. *Compos Part A: Appl Sci Manuf* 2007;38(11):2333–41.
- Sharma AP, Khan SH, Parameswaran V. Experimental and numerical investigation on the uni-axial tensile response and failure of fiber metal laminates. *Compos Part B: Eng* 2017;125:259–74.
- Tarfaoui M, El Moumen A, Lafdi K. Progressive damage modeling in carbon fibers/carbon nanotubes reinforced polymer composites. *Compos Part B: Eng* 2017;112:185–95.
- Alhawamdeh M, Alajarmeh O, Aravinthan T, Shelley T, Schubel P, Mohammed A, et al. Design optimisation of hollow box pultruded FRP profiles using mixed integer constrained Genetic algorithm. *Compos Struct* 2022;302:116247.
- American Society of Civil Engineers. (ASCE). (2010). Pre-Standard for Load and Resistance Factor Design (LRFD) of Pultruded Fiber Reinforced Polymer (FRP) Structures.
- Borowicz DT, Bank LC. Behavior of pultruded fiber-reinforced polymer beams subjected to concentrated loads in the plane of the web. *J Compos Constr* 2011;15(2):229–38.
- Wu C, Bai Y. Web crippling behaviour of pultruded glass fibre reinforced polymer sections. *Compos Struct* 2014;108:789–800.
- Wu C, Zhang LT, Bai Y, Zhao XL. Web crippling behavior of pultruded GFRP channel sections under transverse bearing load. *Compos Struct* 2019;209:129–42.
- Fernandes LA, Gonilha J, Correia JR, Silvestre N, Nunes F. Web-crippling of GFRP pultruded profiles. Part 1: Experimental study. *Compos Struct* 2015;120:565–77.
- Fernandes LA, Nunes F, Silvestre N, Correia JR, Gonilha J. Web-crippling of GFRP pultruded profiles. Part 2: Numerical analysis and design. *Compos Struct* 2015;120:578–90.
- Haloj J, Singh KD, Borsakia AC. Effect of web perforation on the performance of pultruded GFRP wide-flange section profile in web crippling under end-two-flange loading configuration. *Thin-Walled Struct* 2022;175:109187.